

GAFD Special issue on “Recent Developments in Natural Dynamos”

Magnetic Prandtl number dependence of turbulence generated by chiral MHD dynamos

J. SCHOBER, A. BRANDENBURG, I. ROGACHEVSKII, & N. KLEEORIN †*

(Received 00 Month 20xx; final version received 00 Month 20xx)

An asymmetry in the number density of left- and right-handed fermions is known to give rise to a new term in the induction equation that can result in a small-scale instability. This is a microphysical effect characterised by a chiral chemical potential and is mathematically similar to the α effect, which is a turbulent or macrophysical effect. At high temperatures, when a chiral asymmetry can survive for long enough, these chiral MHD dynamos can amplify magnetic fields efficiently, which in turn drive turbulence via the Lorentz force. While it has been demonstrated in numerical simulations that chiral magnetically driven turbulence exists and modifies the evolution of the plasma, the details of this process remain unclear. The goal of this paper is to shed new light on the properties of chiral magnetically driven turbulence using numerical simulations with the PENCIL CODE. We explore the generation of turbulence for different initial conditions, including a variation of the initial chiral chemical potential and the magnetic Prandtl number, Pr_M . In particular, we determine the ratio of kinetic to magnetic energy, Υ^2 , that can be reached in chiral magnetically driven turbulence. Within the parameter space explored in this study, Υ reaches a value of approximately 0.24–0.29—independently of the initial chiral asymmetry and for $\text{Pr}_M = 1$. Our simulations suggest, that Υ decreases as a power law when increasing Pr_M . While the exact scaling depends on the details of the fitting criteria and the Reynolds number regime, an approximate result of $\Upsilon(\text{Pr}_M) = 0.3 \text{Pr}_M^{-0.2}$ is reported. Using the findings from our numerical simulations, we estimate the properties of chiral magnetically driven turbulence in the early Universe.

Keywords: Relativistic magnetohydrodynamics (MHD); Chiral MHD dynamos; Turbulence; Early Universe

1. Introduction

Turbulence and magnetic fields are closely connected in many geophysical and astrophysical flows: Magnetohydrodynamic (MHD) dynamos are often caused by turbulence, so for example in the cases of the small-scale (Kazantsev 1968, Kulsrud and Anderson 1992) and large-scale dynamos, especially those driven by a turbulent α effect (Parker 1955, Steenbeck *et al.* 1966). On the other hand, the Lorentz force resulting from magnetic fields can drive turbulent motions. How much magnetic energy can be converted into kinetic energy depends on various properties of the plasma, characterised by the fluid and magnetic Reynolds numbers, and the structure of the magnetic field. Hence, turbulence is a key ingredient for understanding the origin and evolution of cosmic magnetic fields.

In recent years, the nature of primordial cosmic magnetic fields has been more and more constrained. The lower limits on the strength of intergalactic magnetic fields (Neronov and Vovk 2010, Dermer *et al.* 2011) might be due to possible remains of primordial fields, which can be explained by the following scenario. Seed fields are generated on small spatial scales, below the co-moving Hubble radius of the early Universe, and subsequently cascaded to larger scales in decaying MHD turbulence either with magnetic helicity (Brandenburg *et al.* 1996, Biskamp and Müller 1999, Field and Carroll 2000, Kahniashvili *et al.* 2013, Brandenburg *et al.* 2017a) or without (Brandenburg *et al.* 2015, Zrake 2014). Cosmological seed fields, however, are a

*Email: jennifer.schober@epfl.ch

highly debated topic in modern cosmology, see e.g. Grasso and Rubinstein (2001), Kulsrud and Zweibel (2008), Subramanian (2016), and have been connected to a microphysical effect related to the two opposite handedness of fermions. In the presence of an external magnetic field, the momenta of fermions align along the field lines according to their spin: right-handed fermions move along the field lines, while left-handed ones move in the opposite direction. Consequently, an asymmetry in the number density of left- and right-handed particles leads to a net current along the magnetic field. This effect is called the *chiral magnetic anomaly* (Vilenkin 1980, Redlich and Wijewardhana 1985, Tsokos 1985, Alekseev *et al.* 1998, Fröhlich and Pedrini 2000, 2002, Kharzeev *et al.* 2008, Fukushima *et al.* 2008, Son and Surowka 2009) and the resulting current can lead to a magnetic dynamo instability (Joyce and Shaposhnikov 1997). Especially the studies of the chiral inverse magnetic cascade and the evolution of a non-uniform chiral chemical potential by Boyarsky *et al.* (2012, 2015) who found that a chiral asymmetry can, in principle, survive down to energies of the order of 10 MeV (10^{11} K), made this effect an interesting candidate for cosmological applications.

Recently, a systematic analytical analysis of the system of chiral MHD equations, including the back-reaction of the magnetic field on the chiral chemical potential, and the coupling to the plasma velocity field has been performed by Rogachevskii *et al.* (2017). High-resolution numerical simulations, presented in Schober *et al.* (2017), confirm results from mean-field theory, in particular the existence of a new chiral α effect that is not related to the kinetic helicity, the so-called α_μ effect. Spectral properties of chiral MHD turbulence have been analyzed in Brandenburg *et al.* (2017b). A key result from these direct numerical simulations (DNS) is that turbulence can be magnetically driven by the Lorentz force due to a small-scale chiral dynamo instability. In particular, a new three-stage-scenario of the magnetic field evolution has been found in Schober *et al.* (2017). The small-scale chiral dynamo instability is followed by a phase in which magnetically-produced turbulence triggers a large-scale dynamo instability, which eventually saturates due to the decrease of the chiral chemical potential.

In this paper we extend the work of Schober *et al.* (2017) and explore different initial values of μ and, for the first time, the dependence of the ratio of the kinetic energy over the magnetic energy on the initial chiral asymmetry and the magnetic Prandtl number, $\text{Pr}_M \equiv \nu/\eta$, where ν is the kinematic viscosity and η is the magnetic diffusivity. We also determine the dependence of the kinetic to magnetic energy dissipation rate on the magnetic Prandtl number.

The paper is structured as follows: In section 2, we review the chiral MHD equations, the growth rates of their instabilities, and the saturation magnetic fields expected from the conservation law in chiral MHD. The different stages of chiral magnetically driven turbulence are discussed. The setup of our numerical simulations is described in section 3 and compared with those presented in Schober *et al.* (2017). We discuss the evolution of the velocity field and the magnetic field for a reference run in detail. In section 3.3, we analyze the ratio of kinetic over magnetic energy for different dynamo growth rates and different magnetic Prandtl numbers. In section 4, we estimate the magnetic Prandtl and Reynolds numbers in the relativistic plasma of the early Universe and apply our results on the magnetic Prandtl number dependence.

2. Chiral magnetohydrodynamics

2.1. System of equations

In the following, we review the basic equations of chiral MHD, as derived by Rogachevskii *et al.* (2017). We keep only terms that are linear in the microscopic magnetic diffusivity, η , which is the relevant regime for astrophysical applications. The chiral asymmetry is described

by the chiral chemical potential,

$$\mu_5 = 6(n_L - n_R) \frac{(\hbar c)^3}{(k_B T)^2}, \quad (1)$$

which is proportional to the difference in the number densities of left- and right-chiral fermions, n_L and n_R , respectively. Here, T is the temperature, k_B is the Boltzmann constant, c is the speed of light, and \hbar is the reduced Planck constant. In an external magnetic field, μ_5 gives rise to a current due to the chiral magnetic effect (CME)

$$\mathbf{J}_{\text{CME}} = \frac{\alpha_{\text{em}}}{\pi \hbar} \mu_5 \mathbf{B}, \quad (2)$$

where $\alpha_{\text{em}} \approx 1/137$ is the fine structure constant. This standard model physics effect results in an additional term in the Maxwell equations. Based on these modified Maxwell equations, Boyarsky *et al.* (2015) and Rogachevskii *et al.* (2017) derived the following set of chiral MHD equations:

$$\frac{\partial \mathbf{B}}{\partial t} = \nabla \times [\mathbf{U} \times \mathbf{B} - \eta (\nabla \times \mathbf{B} - \mu \mathbf{B})], \quad (3)$$

$$\rho \frac{D\mathbf{U}}{Dt} = (\nabla \times \mathbf{B}) \times \mathbf{B} - \nabla p + \nabla \cdot (2\nu \rho \mathbf{S}) + \rho \mathbf{f}, \quad (4)$$

$$\frac{D\rho}{Dt} = -\rho \nabla \cdot \mathbf{U}, \quad (5)$$

$$\frac{D\mu}{Dt} = D_5 \Delta \mu + \lambda \eta [\mathbf{B} \cdot (\nabla \times \mathbf{B}) - \mu \mathbf{B}^2] - \Gamma_f \mu, \quad (6)$$

where the magnetic field \mathbf{B} is normalized such that the magnetic energy density is $\mathbf{B}^2/2$ (so the magnetic field in Gauss is $\sqrt{4\pi} \mathbf{B}$), and $D/Dt = \partial/\partial t + \mathbf{U} \cdot \nabla$ is the advective derivative. Further, a normalization of μ_5 is used such that $\mu = (4\alpha_{\text{em}}/\hbar c)\mu_5$ and the chiral feedback parameter λ has been introduced, which characterizes the strength of the back-reaction from the electromagnetic field on the evolution of μ . For hot plasmas, when $k_B T \gg \max(|\mu_L|, |\mu_R|)$, it is given by (Boyarsky *et al.* 2015)

$$\lambda = 3\hbar c \left(\frac{8\alpha_{\text{em}}}{k_B T} \right)^2. \quad (7)$$

In equations (3)–(6), D_5 is a chiral diffusion coefficient, p is the fluid pressure, $S_{ij} = \frac{1}{2}(U_{i,j} + U_{j,i}) - \frac{1}{3}\delta_{ij}\nabla \cdot \mathbf{U}$ are the components of the trace-free strain tensor, where commas denote partial spatial differentiation, ν is the kinematic viscosity, and \mathbf{f} is the turbulent forcing function. For an isothermal equation of state, the pressure p is related to the density ρ via $p = c_s^2 \rho$, where c_s is the isothermal sound speed. The last term in equation (6) describing the chiral flipping reactions at a rate Γ_f is neglected in this work, because we consider situations where it is subdominant in comparison with the remaining terms.

The system of equations is determined by several non-dimensional parameters. In terms of chiral MHD dynamos, the most relevant ones are the chiral Mach number

$$\text{Ma}_\mu = \frac{\eta \mu_0}{c_s} \equiv \frac{v_\mu}{c_s}, \quad (8)$$

and the dimensionless chiral nonlinearity parameter:

$$\lambda_\mu = \lambda \eta^2 \bar{\rho}. \quad (9)$$

The parameter Ma_μ measures the relevance of the chiral term in the induction equation (3) and determines the growth rate of the small-scale chiral dynamo instability. The nonlinear back reaction of the magnetic field on the chiral chemical potential μ is characterized by λ_μ , which

affects the strength of the saturation magnetic field and the strength of the magnetically driven turbulence. In this paper we consider only cases with $\lambda_\mu \ll 1$, i.e., when turbulence is produced efficiently due to strong magnetic fields generated by the small-scale chiral dynamo instability. The turbulent cascade properties have previously been studied by Brandenburg *et al.* (2017b) in the range $2 \times 10^{-6} \leq \lambda_\mu \leq 200$, Schober *et al.* (2017) in the range $10^{-9} \leq \lambda_\mu \leq 10^{-5}$.

2.2. Analogy with the α effect in mean-field electrodynamics

Readers familiar with mean-field electrodynamics (MFE, see Moffatt 1978, Krause and Rädler 1980) will have readily noticed the analogy between $v_\mu = \mu \eta$ in chiral MHD and the α in MFE. For $\eta \rightarrow 0$, the analogy goes further in that even the evolution equation (6) for μ corresponds to an analogous one for α in what is known as the dynamical quenching formalism (Kleeorin and Ruzmaikin 1982). In chiral MHD, this implies that the total chirality is conserved. In MFE, it implies that the total magnetic helicity is conserved, i.e., the sum of the magnetic helicity of the mean-field and that of the fluctuating or small-scale field, the latter of which constitutes an additional time-dependent contribution to the α effect. The other contribution to the α effect in MFE is proportional to the kinetic helicity, which was here assumed to be constant in time, so we can write (see equation 18 of Blackman and Brandenburg 2002)

$$\frac{\partial \alpha}{\partial t} = \lambda_{\text{MFE}} \eta \left[\eta_\tau \overline{\mathbf{B}} \cdot (\nabla \times \overline{\mathbf{B}}) - \alpha \overline{\mathbf{B}}^2 \right] - \Gamma_{\text{MFE}} (\alpha - \alpha_K), \quad (10)$$

where η_τ is the turbulent magnetic diffusivity. In MFE, the coupling coefficient is given by $\lambda_{\text{MFE}} = 2\eta_\tau k_f^2 / (\eta B_{\text{eq}}^2)$ and $\Gamma_{\text{MFE}} = 2\eta k_f^2$, where k_f is the wavenumber of the energy-carrying eddies and B_{eq} is the equipartition field strength.

The applications of chiral MHD carry over to decaying MHD turbulence with finite initial large-scale or small-scale magnetic helicity (Kemel *et al.* 2011). During the decay, some of the magnetic helicity is transferred between the large- and small-scale fields, which leads to a change in the α effect that in turn results in a slow-down of the decay.

2.3. Review of the three stages of chiral magnetically driven turbulence

Recent simulations by Schober *et al.* (2017) have demonstrated the existence of three distinct stages characterizing the growth and saturation of chiral magnetically driven dynamos. The purpose of this section is to assess and discuss potential restrictions arising from finite size effects associated with the computational domain. We begin with a schematic overview of a chiral MHD dynamo as presented in figure 1. It shows the evolution of an initially weak magnetic seed field in the presence of a chemical potential with an initial value μ_0 . We consider here the case of a small nonlinearity parameter λ_μ , which allows for an extended dynamo phase with enough time for the excitation of turbulent motions. Based on the evolution of the magnetic field, Schober *et al.* (2017) distinguish three different phases:

Phase 1: a laminar small-scale chiral dynamo instability;

Phase 2: a large-scale dynamo instability, caused by chiral magnetically produced turbulence;

Phase 3: termination of growth of the large-scale magnetic field and reduction of μ according to the conservation law in chiral MHD.

With no further energy input, dynamo saturation is followed by decaying helical MHD turbulence, where the magnetic field decreases with time as a power law like $|\mathbf{B}| \sim t^{-1/3}$ (Biskamp and Müller 1999, Kahniashvili *et al.* 2013).

2.3.1. Laminar and turbulent dynamo amplification

In **phase 1**, the velocity field is negligible and a small-scale laminar dynamo operates. The growth rate found from the linearized equation (3) has a maximum value of (Rogachevskii

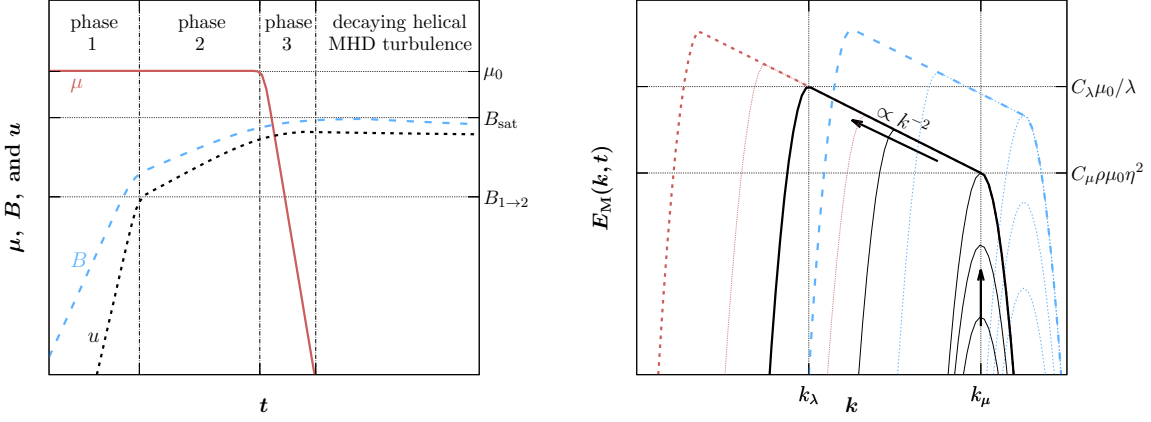


Figure 1. *Left panel:* Schematic overview of the evolution an initially weak magnetic field in the presence of a chiral chemical potential. The time evolution of μ is presented as the red line, the one of u as the black line, and the one of B as the blue line. Further, the initial value of the chiral chemical potential, μ_0 , and the saturation value of the magnetic field strength, $(\mu_0/(\lambda\xi_M))^{1/2}$, are indicated as horizontal dotted lines. The transitions between individual phases of the evolution are marked by black dashed-dotted lines and discussed in section 2.3. *Right panel:* Evolution of magnetic energy spectra, where the maximum growth rate of the chiral dynamo is located at the wavenumber k_μ (black lines around the vertical arrow). Eventually, the peak of the spectrum moves to smaller wavenumbers for $E_M > C_\mu \rho \mu_0 \eta^2$ and reaches its maximum value $E_M = C_\lambda \mu_0 / \lambda$ at k_λ , while still being supplied by energy from the wavenumber $k = \mu/2$ through inverse cascading along a k^{-2} spectrum. Characteristic values of the wavenumber and the spectral energy are only indicated at the axes for the black spectra. The blue lines show a case with a larger μ_0 than for the black lines (but the same λ) and the red lines a case with a smaller λ (but the same μ_0) than for the black lines. Thin lines show intermediate spectra, while thick lines show the spectra when the magnetic energy has reached its maximum value.

et al. 2017)

$$\gamma_\mu = \frac{v_\mu^2}{4\eta} \quad (11)$$

being attained at

$$k_\mu = \frac{|\mu_0|}{2}. \quad (12)$$

During this phase, turbulence is driven by the Lorentz force with the rms velocity increasing at a rate of approximately $2\gamma_\mu$.

In **phase 2**, the turbulent velocity field has become so strong that it affects the evolution of the magnetic field. It has been shown by Brandenburg *et al.* (2017b) that the peak of the magnetic energy spectrum reaches a value of

$$E_M^{1 \rightarrow 2} = C_\mu \bar{\rho} \mu_0 \eta^2 \quad (13)$$

with $C_\mu \approx 16$ at the transition from phase 1 to phase 2. This moment coincides with the beginning of the inverse transfer, when the k^{-2} spectrum starts to build up, i.e. when the peak of the magnetic energy spectrum moves from k_μ to smaller wavenumbers. The corresponding transition field strength can be estimated as

$$B_{\text{rms}}^{1 \rightarrow 2} \approx (E_M^{1 \rightarrow 2} k_\mu)^{1/2} \approx \left(\frac{C_\mu \bar{\rho}}{2} \right)^{1/2} \mu_0 \eta. \quad (14)$$

Rogachevskii *et al.* (2017) have studied the evolution of the large-scale magnetic using a mean-field approach. They find that the maximum growth rate of the field strength reaches a value of

$$\gamma_\alpha = \frac{(\bar{v}_\mu + \alpha_\mu)^2}{4(\eta + \eta_T)} = \frac{(\bar{v}_\mu + \alpha_\mu)^2}{4\eta(1 + \text{Re}_M/3)}. \quad (15)$$

Despite the contribution from the chiral α effect, given by the term $\alpha_\mu = -\frac{2}{3}\bar{v}_\mu \ln \text{Re}_M$, the overall growth rate is reduced as compared to the laminar dynamo. Here, Re_M is the magnetic Reynolds number defined by $\text{Re}_M = u_0 \ell_0 / \eta = 3\eta_T / \eta$ and η_T is the turbulent magnetic diffusivity. The maximum growth rate of the large-scale chiral dynamo is attained at the wavenumber $k_\alpha = |\bar{v}_\mu + \alpha_\mu| / (2\eta + 2\eta_T)$.

2.3.2. Saturation magnetic field

Saturation of the chiral dynamo, **phase 3**, is determined by the conservation law following from equations (3)–(6), which implies that the total chirality

$$\frac{\lambda}{2} \overline{\mathbf{A} \cdot \mathbf{B}} + \bar{\mu} = \mu_0 = \text{const}, \quad (16)$$

is a conserved quantity; see Rogachevskii *et al.* (2017) for more details. Here, $\bar{\mu}$ is the spatially averaged value of the chemical potential and $\overline{\mathbf{A} \cdot \mathbf{B}}$ is the magnetic helicity. According to the conservation law (16), the magnetic field reaches $B_{\text{sat}} = (\mu_0 / (\lambda \xi_M))^{1/2}$, where ξ_M is the correlation length of the magnetic field.

The magnetic energy spectrum $E_M(k, t)$ in chiral MHD turbulence has been studied in Brandenburg *et al.* (2017b). In particular, it was found that E_M is proportional to k^{-2} between the wavenumber

$$k_\lambda = \sqrt{\bar{\rho} \lambda \frac{C_\mu}{C_\lambda} \eta \mu_0}, \quad (17)$$

with $C_\mu \approx 16$, $C_\lambda \approx 1$, and k_μ given by equation (12). We note that the only case considered here is $\lambda_\mu \ll 1$, which implies $k_\lambda \ll k_\mu$. Using dimensional arguments and numerical simulations, Brandenburg *et al.* (2017b) found that for chiral magnetically driven turbulence, the saturation magnetic energy spectrum $E_M(k, t)$ obeys

$$E_M(k, t) = C_\mu \bar{\rho} \mu_0^3 \eta^2 k^{-2} \quad (18)$$

in $k_\lambda < k < \mu_0$. Here, $E_M(k, t)$ is normalized such that the mean magnetic energy density is $\langle \mathbf{B}^2 \rangle / 2 = \int E_M(k) dk$. It was also confirmed numerically by Brandenburg *et al.* (2017b) that the magnetic energy spectrum $E_M(k)$ is limited from above by $C_\lambda \mu_0 / \lambda$, where $C_\lambda \approx 1$ is another empirical constant. The magnetic field strength at dynamo saturation can be estimated as

$$B_{\text{sat}} \approx (E_M(k_\lambda) k_\lambda)^{1/2} = \left(\frac{\bar{\rho} \eta^2 C_\mu C_\lambda}{\lambda} \right)^{1/4} \mu_0. \quad (19)$$

In the right panel of figure 1 the effect of changing μ_0 and λ on the final energy spectrum is illustrated. Here, intermediate spectra are shown as thin lines, while thick lines indicate the magnetic energy spectrum at saturation with an inertial range where $E_M \propto k^{-2}$ between k_λ and k_μ . The black lines present a case with a certain μ_{black} and λ_{black} . If λ is decreased, k_λ decreases, too, and the k^{-2} spans over a larger range of wavenumbers. This is illustrated in the case shown with red lines where $\mu_{\text{red}} = \mu_{\text{black}}$ and $\lambda_{\text{red}} < \lambda_{\text{black}}$. In the scenario illustrated by red color, the final magnetic field strength is higher than in the case with μ_{black} and λ_{black} . The same final field strength can, however, also be reached by increasing μ_0 , as $B_{\text{sat}} \propto \mu_0 / \lambda^{1/4}$. Schematic spectra illustrating the latter case are shown as blue curves in figure 1, where $\mu_{\text{blue}} > \mu_{\text{black}}$ and $\lambda_{\text{blue}} = \lambda_{\text{black}}$.

2.4. Effects from the finite numerical domain

Due to the finiteness of the simulation domain, the evolution of the magnetic field and turbulence is slightly modified in comparison to the scenario discussed in section 2.3. The evolution

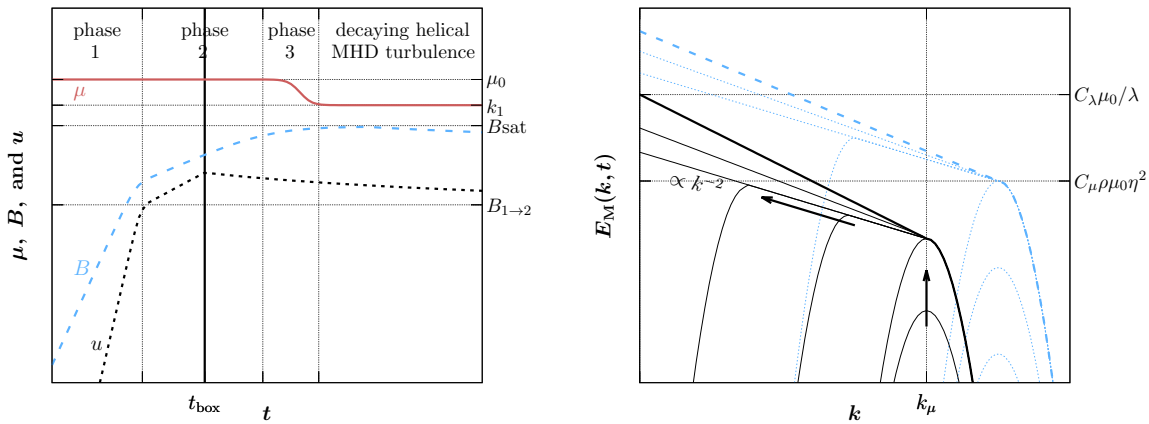


Figure 2. Same as figure 1 but including effects of a finite box. *Left panel:* Time evolution of various quantities. *Right panel:* Evolution of magnetic energy spectra. The blue curves show an example with larger initial μ_0 as compared to the black curves.

of the chemical potential, the magnetic field strength, and the velocity, as well as the time evolution of the magnetic energy spectrum in finite box simulations is illustrated in figure 2.

First of all, the chemical potential does not vanish at dynamo saturation, but reaches a finite value, which is equal to the minimum wavenumber possible in the box, k_1 . The magnetic field reaches the saturation value given in equation (19). However, the evolution of the magnetic energy spectrum differs as compared to an infinite system. In the laminar dynamo phase, we expect an instability on the scale k_μ , as predicted by theory; see the black curves in the right panel of figure 2. With the onset of turbulence, the peak of the energy spectrum moves to larger spatial scales through inverse transfer. As discussed above, we expect a scaling of the magnetic energy spectrum proportional to k^{-2} ; see equation (18). Once, the peak reaches the size of the box, however, we observe a steepening of the spectrum, as indicated in the schematic figure 2. This steepening is caused by the growth of the magnetic field on the smallest possible wavenumber, until the spectrum reaches its saturation value $C_\lambda \mu_0 / \lambda$. For large values of μ_0 the initial instability occurs on smaller spatial scales, i.e. larger k , and thus the k^{-2} spectrum can extend over a larger range; see the blue curves in the right panel of figure 2.

When $k_\lambda < k_1$, we no longer expect the evolution of the magnetic energy spectrum to be as presented in the right panel of figure 1. For studies of mean field chiral dynamos, however, large scale separation $k_\lambda \gg k_\mu$ is required which in turn is only possible for extremely high resolution. In this paper, we present only one run with $k_\lambda \approx k_1$, Run B, which has a resolution of 1216^3 . Large parameter scans, and cases with an additional large scale separation $k_\lambda \gg k_1$ are computationally too expensive.

3. Chiral magnetically driven turbulence in direct numerical simulations

3.1. Numerical setup

We solve equations (3)–(6) in a three dimensional periodic box of size $L^3 = (2\pi)^3$ with the PENCIL CODE¹. This code is well suited for MHD studies; it employs a third-order accurate time-stepping method and sixth-order explicit finite differences in space (Brandenburg and Dobler 2002, Brandenburg 2003). The smallest wavenumber covered in the numerical domain is $k_1 = 2\pi/L = 1$ and the resolution is varied between 480^3 and 1216^3 . Some of these simulations

¹<http://pencil-code.nordita.org/>

Table 1. Overview of the simulations discussed in this paper. Runs C, D, and E have been repeated with different magnetic Prandtl numbers, i.e. Run C05 has $\text{Pr}_M = 0.5$, Run C1 has $\text{Pr}_M = 1$, up to Run C10 with $\text{Pr}_M = 10$. Reference runs are highlighted by bold font.

simulation	resolution	Ma_μ	λ_μ	$(\mu_0/\lambda)^{1/2}$	k_μ/k_1	k_λ/k_1	Pr_M
Run A	576³	2×10^{-3}	2×10^{-7}	1.00	10	0.036	1.0
Run B	1216 ³	6.6×10^{-3}	9×10^{-6}	0.12	44	1.1	1.0
Run C	480 ³	1.5×10^{-3}	5×10^{-6}	0.12	15	0.27	1.0
Runs D05...10	480³	2×10^{-3}	5×10^{-6}	0.14	20	0.36	0.5...10
Run E	480 ³	2.5×10^{-3}	5×10^{-6}	0.16	25	0.45	1.0
Runs F1...10	576 ³	3×10^{-3}	5×10^{-6}	0.17	30	0.54	0.5...10
Runs G05...10	480 ³	4×10^{-3}	2×10^{-5}	0.14	20	0.72	0.5...10
Runs H05...10	480 ³	8×10^{-3}	2×10^{-5}	0.28	20	0.72	0.5...10

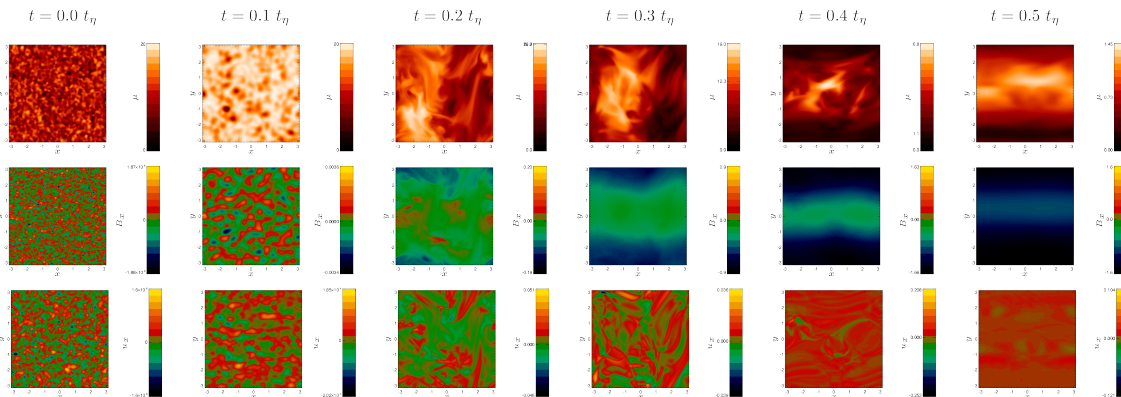


Figure 3. xy cross sections of the chemical potential (μ , top row), as well as the x components of the magnetic field (B_x , middle row), and the velocity field (u_x , bottom row) in the xy plane. From left to right the time increases from 0 to $0.5 t_\eta$, during which the chiral MHD dynamo generates a large-scale magnetic field and a velocity field.

have already been presented previously (Schober *et al.* 2017), but we now include additional runs for $\text{Pr}_M \neq 1$. The sound speed in the simulations is set to $c_s = 1$ and the mean fluid density to $\bar{\rho} = 1$. If not indicated otherwise, the magnetic Prandtl number is 1, i.e. the magnetic diffusivity equals the viscosity. However, we do consider cases between $\text{Pr}_M = 0.5$ and $\text{Pr}_M = 10$, where the value of η is fixed and ν changes. No external forcing is applied to drive turbulence in the simulations, i.e. the velocity field is then driven entirely by magnetic fields. All runs are initialized with a weak magnetic seed field in form of Gaussian noise, with constant μ , and vanishing velocity.

The main parameters of all simulations presented in this paper are summarized in table 1.

3.2. Reference run for chiral magnetically driven turbulence

The generation of a mean field for a representative chiral MHD dynamo (Run A) can be seen in figure 3, where we present snapshots of μ (top row), B_x (middle row), and u_x (bottom row) for the reference run, Run A. As indicated at the top, from left to right the time increases from $t = 0$ to $t = 0.5 t_\eta$, where the Ohmic diffusion time is defined as $t_\eta \equiv (\eta k_1^2)^{-1}$. In the following, we summarize the quantitative analysis of Run A, but we refer to section 4 of Schober *et al.* (2017) for a more detailed discussion of this simulation.

The time evolution of the central MHD quantities for the reference Run A is shown in figure 4. As can be seen in the left panel, B_{rms} (black solid line) increases exponentially by over 4 orders of magnitude before the growth rate decreases due to the generated turbulence. Saturation occurs at $t \approx 0.4 t_\eta$. Both, the velocity u_{rms} (gray dashed line) and the magnetic

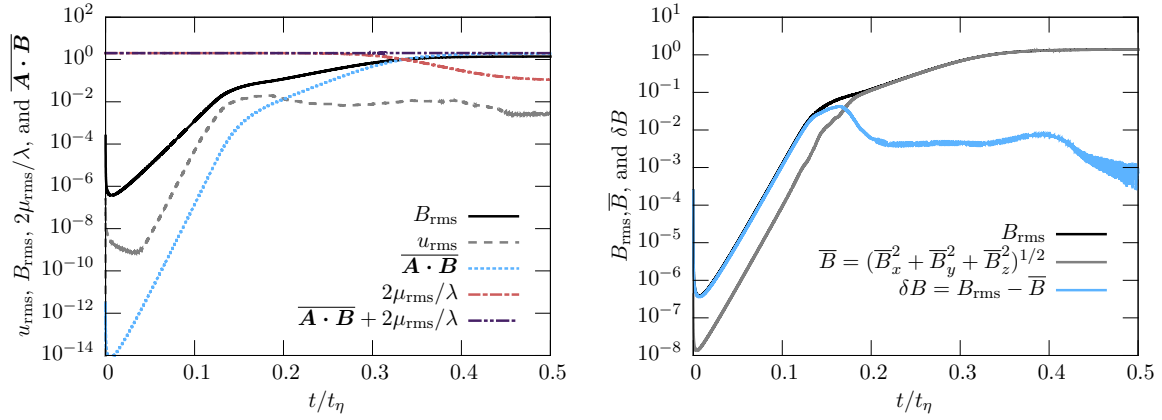


Figure 4. The time evolution of the most relevant parameters in the reference run, Run A. This run has been discussed in greater detail in section 4 of Schober *et al.* (2017). The left panel above is equivalent to the top panel of their figure 9.

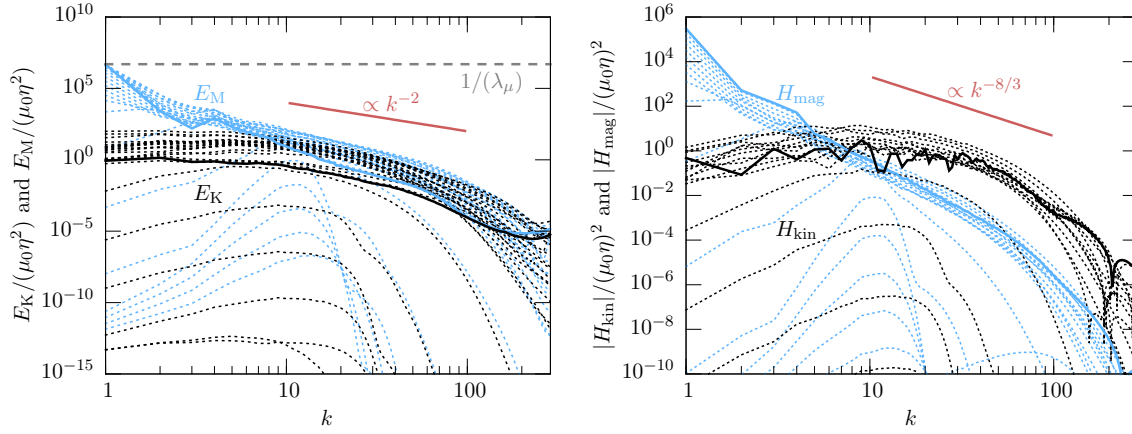


Figure 5. Normalized energy and helicity spectra for the reference run, Run A. The time intervals between two spectra are equidistant and the last spectra are presented by solid lines. The left panel above is equivalent to figure 10 of Schober *et al.* (2017).

helicity $\overline{\mathbf{A} \cdot \mathbf{B}}$ (blue dotted line) increase at a rate twice the one of B_{rms} . The value of μ_{rms} (orange dashed-dotted line), here shown with a constant factor $2/\lambda$, decreases above $t \approx 0.3 t_\eta$, switching off the dynamo instability. In accordance with the conservation law (16), the sum $\overline{\mathbf{A} \cdot \mathbf{B}} + 2\mu_{\text{rms}}/\lambda$ (purple dashed-dotted line) is constant throughout the simulation time. In the right panel of figure 4, it can be seen that the magnetic field is initially dominated by fluctuations (blue line). During the mean-field dynamo phase a large-scale field (gray line) is produced.

The kinetic and magnetic energy (left panel) and helicity spectra (right panel) are presented in figure 5. All spectra grow from initially low values and the final spectra are presented as solid lines. From here we confirm that the laminar chiral dynamo injects energy at the wavenumber k_μ , as given in equation (12). Once turbulence has been generated, the magnetic correlation length moves to smaller wavenumbers.

3.3. Turbulence in different scenarios

In the analysis of the reference Run A, we have seen that the kinetic energy reaches a certain percentage of the magnetic energy. With the onset of the turbulent dynamo phase, phase 2,

the ratio

$$\Upsilon \equiv \left(\frac{\rho u_{\text{rms}}^2/2}{B_{\text{rms}}^2/2} \right)^{1/2} \quad (20)$$

stays approximately constant and decreases as soon as the peak of the magnetic energy spectrum reaches the box wavenumber k_1 . Afterwards, turbulence is not driven by the Lorentz force anymore and the plasma enters the regime of decaying MHD turbulence.

In this section we explore how the details of this scenario are effected by the properties of the plasma. Therefore, we study a broad parameter space, varying the chiral parameters as well as the magnetic Prandtl number.

3.3.1. Dependence on the chiral parameters Ma_μ and λ_μ

The time evolution of Υ is presented in the left panel of figure 6 for runs with different values of Ma_μ and λ_μ . Time is normalized here by the inverse of the laminar dynamo growth rate (11), allowing a better comparison between runs with different v_μ . The evolution up to $t \approx 12 \gamma_\mu^{-1}$ of all runs is similar, except for a minor time delay of Run A. This can be explained by the magnetic diffusivity which is larger than the one in Run C by a factor of two. Phase 2, when turbulence affects the evolution of the magnetic field, begins approximately at $t \approx 12 - 14 \gamma_\mu^{-1}$ for the runs considered here. The onset of phase 2 is weakly dependent on η and, in principle, also on the initial value of the magnetic field strength, which is the same for all runs presented in this paper. During phase 2, the ratio Υ is comparable for all 3 runs considered here, even though Ma_μ and λ_μ are different. Once the mean-field dynamo phase begins, we observe a ratio $\Upsilon \approx 0.2-0.3$.

Run A, the reference run discussed in the previous section, has the lowest value of λ in our sample, leading to a small value of k_λ in comparison to the maximum wavenumber in the box: $k_\lambda \approx 0.036 k_1$. This implies that k_1 is reached early, much before dynamo saturation, and the kinetic energy decays. The line style of the curves in the left panel of figure 6 is changed from solid to dashed at the time when $k_M = k_1$ is reached. For a scenario in which the inverse cascade takes place completely inside the box, and hence kinetic energy does not decay within phase 2, we have performed Run B. The choice of the parameters for this run, listed in table 1, can be justified as follows: As for all of the runs presented in this paper, the ratio between k_μ and k_λ needs to be large, in order to observe a turbulent dynamo phase (phase 2). Using equations (12) and (17), we see that

$$\frac{k_\mu}{k_\lambda} = \left(\frac{C_\lambda}{4C_\mu} \frac{1}{\bar{\rho}\eta^2\lambda} \right)^{1/2} = \left(\frac{C_\lambda}{4C_\mu} \frac{1}{\lambda_\mu} \right)^{1/2}, \quad (21)$$

which is independent of μ_0 . However, μ_0 needs to be chosen high enough to ensure that $k_\lambda > k_1$. Here we use $\mu_0/k_1 = 88$, which implies that the laminar dynamo instability occurs on small spatial scales and a high numerical resolution is required. Run B is presented in the left panel of figure 6 as a gray solid line, for which the ratio Υ remains approximately constant for times larger than $\approx 12 \gamma_\mu^{-1}$.

In the right panel of figure 6, we show the time averaged ratio $\langle \Upsilon \rangle_t$ for all our runs with $\text{Pr}_M = 1$ as a function of μ_0/k_1 as black data points. The blue data points refer to the upper x axes and indicate the corresponding value of Ma_μ . For the time averaging procedure, we consider two different criteria: For solid data points the time average is performed for all values of Υ larger than 50% of its maximum value. The open dots are obtained by using all values for which $\Upsilon > 0.9 \max(\Upsilon)$, which obviously results in a larger average value. Error bars represent the standard deviation of $\langle \Upsilon \rangle_t$. There is no significant dependence of $\langle \Upsilon \rangle_t$ on the values of μ_0 and Ma_μ for the parameter space explored here: When averaging over all $\Upsilon > 0.5 \max(\Upsilon)$ we find a mean $\langle \Upsilon \rangle_t \approx 0.24 \pm 0.01$ and when employing the criterion $\Upsilon > 0.9 \max(\Upsilon)$ we find $\langle \Upsilon \rangle_t \approx 0.27 \pm 0.01$.

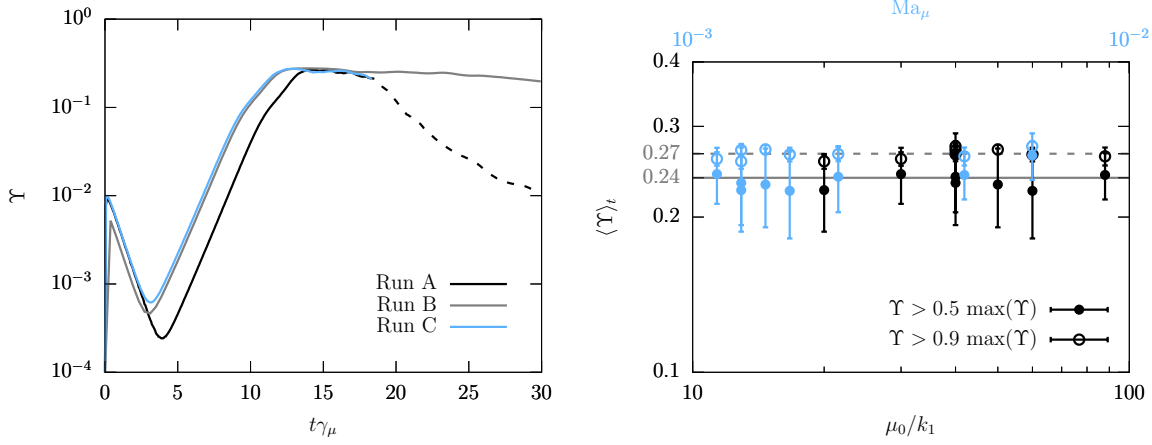


Figure 6. *Left panel:* The square root of the ratio of kinetic over magnetic energy, Υ , as a function of time, normalized by the inverse laminar dynamo growth rate γ_μ as given in equation (11), for Runs A–C with $\text{Pr}_M = 1$ and different values of the chiral Mach number and the nonlinearity parameter; see table 1. The time during which k_M is inside the numerical box, i.e., $k_M > k_1$, is marked by solid line style. For $k_M < k_1$, the lines are dashed. *Right panel:* The time averaged ratio Υ as a function of μ_0/k_1 (lower abscissa, black data points) and a function of Ma_μ (upper abscissa, blue data points) for all runs with $\text{Pr}_M = 1$. For the results shown as filled dots, the average has been performed for the time interval for which Υ is at least 50% of its maximum value. For open dots, the time average is taken for all $\Upsilon > 0.9 \max(\Upsilon)$. The solid gray line shows the mean value of $\langle \Upsilon \rangle_t$ resulting from the first time averaging condition and the dashed gray for the latter condition.

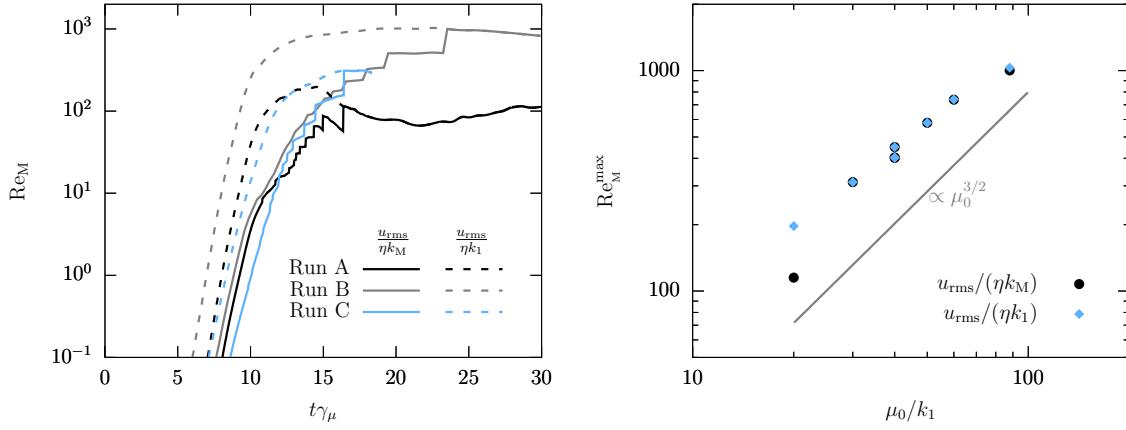


Figure 7. *Left panel:* The magnetic Reynolds number Re_M as a function of time for Runs A – C. The solid lines indicate the result using k_M as the integral scale of turbulence and dashed lines show the result using k_1 . At late times $k_M = k_1$ in our DNS, which are confined within a finite box. *Right panel:* The maximum magnetic Reynolds number found in our simulations versus μ_0/k_1 , for both cases $Re_M = u_{\text{rms}}/(\eta k_1)$ (black dots) and $Re_M = u_{\text{rms}}/(\eta k_M)$ (blue diamonds). The solid line indicates the scaling $\mu_0^{3/2}$ which is expected for finite box simulations with $k_{\text{box}} > k_\lambda$.

Knowing the amount of turbulent kinetic energy that can be produced by Lorentz force driving, is essential for estimating the Reynolds number in the plasma. The latter is determined by the rms velocity, the magnetic diffusivity, and the correlation length of the magnetic field. In numerical simulations, both u_{rms} and k_M can be limited by the size of the box, while η is an input parameter. We have seen that $\langle \Upsilon \rangle_t$ has an approximately fixed value in the mean-field dynamo phase for $\text{Pr}_M = 1$ and as long as $k_M > k_1$. This implies that the value of u_{rms} is proportional to B_{rms} and reaches a maximum at the time t_{box} , which is defined as the time when the peak of the energy spectrum reaches the size of the box, i.e., when $k_M = k_1$. The energy spectrum at this time is given by equation (18) and has a maximum value of $E_M(k_1, t_{\text{box}}) = C_\mu \bar{\rho} \eta^2 \mu_0^3 / 2$. The magnetic field strength corresponding to this energy spectrum

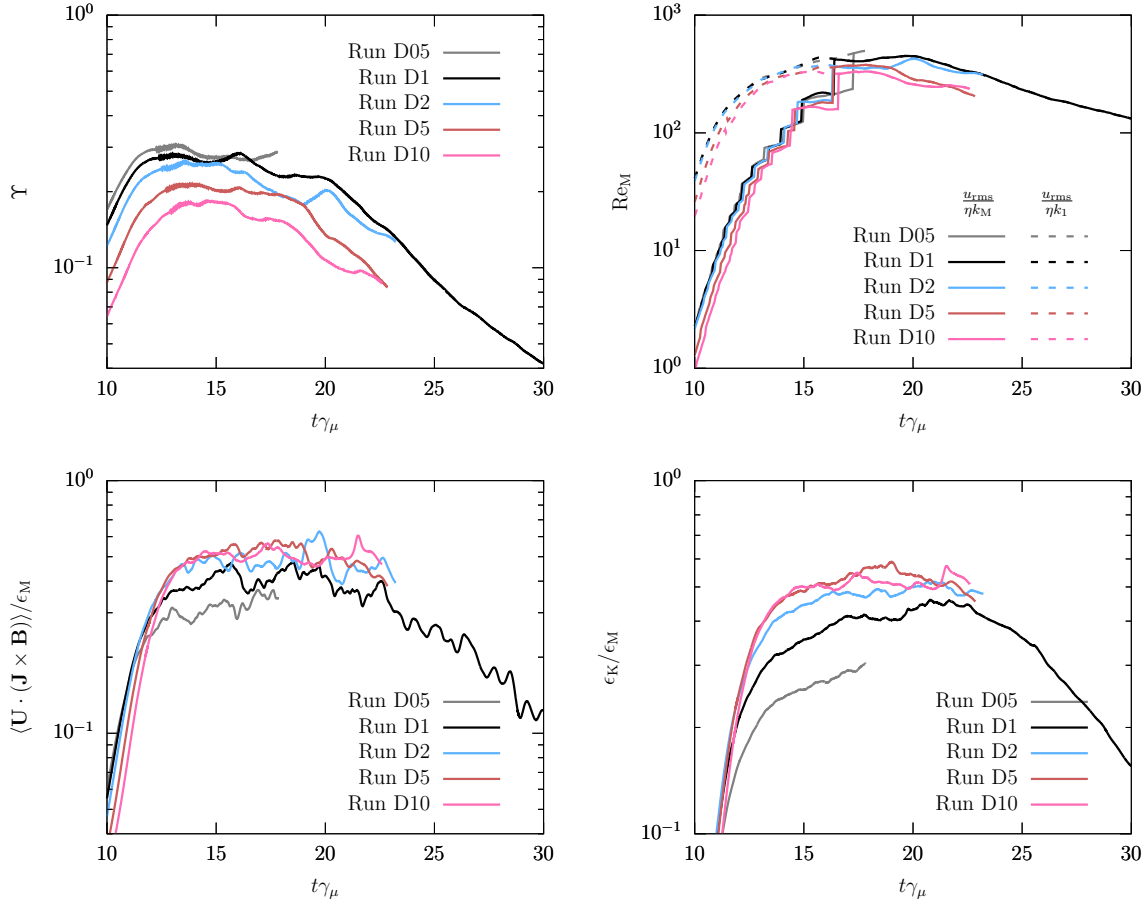


Figure 8. *Top left panel:* Rms velocity over magnetic field strength as a function of time for Run series D (see table 1), in which the magnetic Prandtl number is varied between $Pr_M = 0.5$ (Run D05) and $Pr_M = 10$ (Run D10), respectively, through variation of the viscosity. Time is normalized by the inverse laminar dynamo growth rate γ_μ given in equation (11). The simulation time during which k_M is inside the numerical box, i.e., $k_M > k_1$, is marked by solid line style. For $k_M < k_1$, the lines are dashed. *Top right panel:* The magnetic Reynolds number Re_M as a function of time for Run series D. The solid lines indicate the result using k_M as the integral scale of turbulence and dashed lines show the result using k_1 . *Bottom left panel:* The mean work done against the Lorentz force, $\langle \mathbf{U} \cdot (\mathbf{J} \times \mathbf{B}) \rangle$, divided by Joule dissipation, ϵ_M , as a function of time for Run series D. *Bottom right panel:* The ratio of viscous over Joule dissipation, ϵ_K/ϵ_M , measured in our simulations.

can be estimated as $(E_M(k_1, t_{\text{box}})k_1)^{1/2} = (C_\mu \bar{\rho}/2)^{1/2} \eta \mu_0^{3/2}$. Hence we expect a scaling of the maximum velocity in our simulations $\propto \eta \mu_0^{3/2}$. The Reynolds number, $Re_M = u_{\text{rms}}/(\eta k_M)$ with $k_M = k_1$ at late times, is thus independent of η and scales $\propto \mu_0^{3/2}$. This scaling is observed in our simulations; see the right panel of figure 7. The Reynolds number as a function of time for runs with different μ_0/k_1 is presented in the left panel of this figure. Here, we show two different ratios, $u_{\text{rms}}/(\eta k_M)$ and $u_{\text{rms}}/(\eta k_1)$. For the first case, k_M is measured as a function of time using the magnetic energy spectra. At late times, once the peak of the magnetic energy spectrum has reached the box wavenumber, $k_M = k_1$, and the dashed and solid curves for individual runs coincide.

3.3.2. Dependence on the magnetic Prandtl number

We have performed series of runs with different magnetic Prandtl numbers by changing the value of the kinetic viscosity, in order to explore any trends of the conversion of magnetic to kinetic energy. In the top left panel of figure 9 the time evolution for the ratio Υ is shown for run series D. Here, Pr_M increases from 0.5 (gray line) up to 10 (orange line), while all other

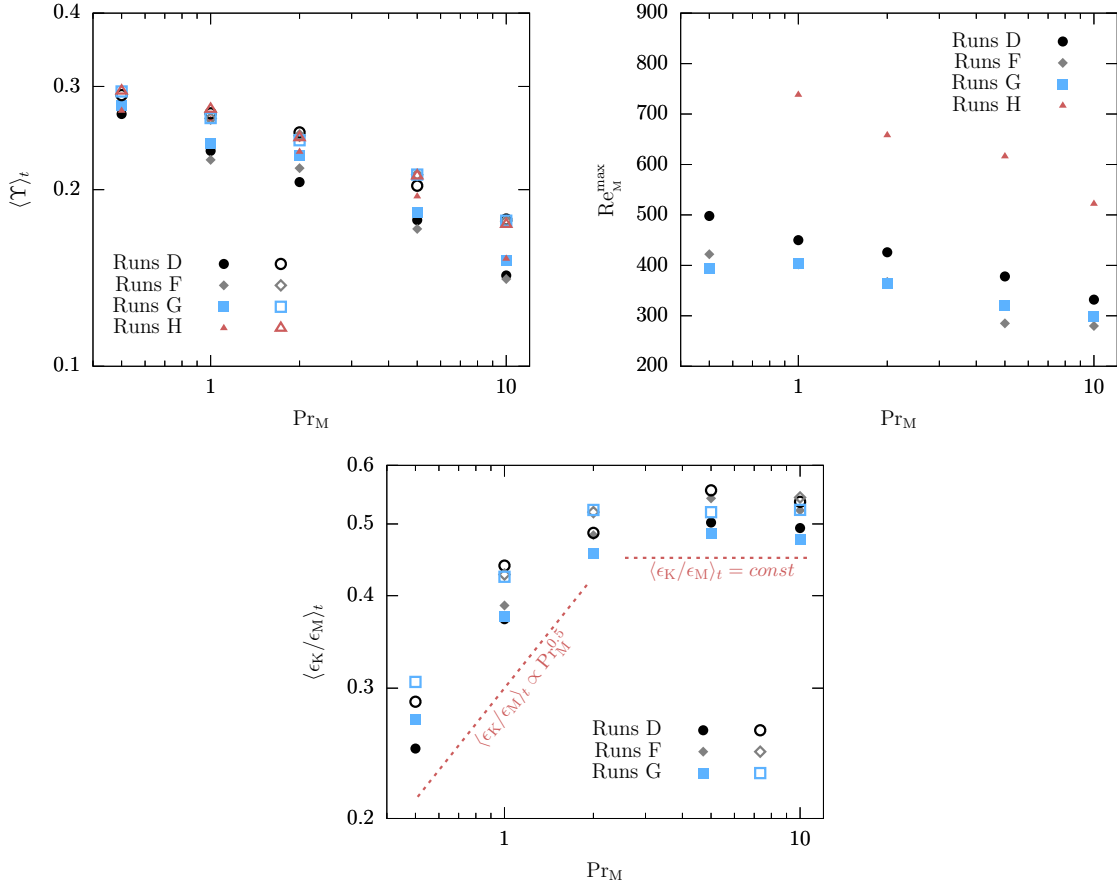


Figure 9. *Top left panel:* The time averaged value of Υ for different run series. Filled symbols represent the result from an time averaging of all data points with $\Upsilon > 0.5 \max(\Upsilon)$ and open symbols averaging is performed for all data with $\Upsilon > 0.9 \max(\Upsilon)$. Errors are of the order of 10% for the filled symbols and 5% for the open symbols, but not presented in the figure for better visualization. *Top right panel:* The maximum magnetic Reynolds number in the different DNS as a function of Pr_M . *Bottom panel:* The time averaged ratio of viscous over Joule dissipation, $\langle \epsilon_K / \epsilon_M \rangle_t$, as a function of Pr_M . Again, for filled data points, the average of ϵ_K / ϵ_M is calculated for all values $\epsilon_K / \epsilon_M > 0.5 \max(\epsilon_K / \epsilon_M)$ and for open data points averaging is performed for $\epsilon_K / \epsilon_M > 0.9 \max(\epsilon_K / \epsilon_M)$.

run parameters are unchanged; for details see table 1. The most important conclusion from the top left panel of figure 9 is that Υ decreases significantly with increasing Pr_M .

It should be noted that low Pr_M are difficult to obtain in DNS at fixed η , as an increase of resolution is required when decreasing ν . Run D05, for example, crashes at $t \approx 17 \gamma_\mu^{-1}$ as a result of a too large mesh Reynolds number. There is sufficient data for phase 2 available for this run to include it the $Pr_M = 0.5$ runs in our analysis. However, a quantitative study of the low Prandtl number regime is inaccessible to our current simulations and beyond the scope of this paper.

The maximum magnetic Reynolds numbers, Re_M^{\max} , obtained in Runs D are presented in the top right panel of figure 9. It can be seen that a dependence of Re_M^{\max} on Pr_M exists, which is caused by the decrease of u_{rms} for increasing Pr_M . As discussed in the previous section, a change of Re_M in DNS with $k_\lambda < k_1$ can only be achieved by changing μ_0 . In the bottom panels of figure 8, we present the time evolution of two more quantities describing the energy flow from kinetic to magnetic energy. We find that both, the work done by the Lorentz force, $\langle \mathbf{U} \cdot (\mathbf{J} \times \mathbf{B}) \rangle$, and the ratio of viscous over Joule dissipation, ϵ_K / ϵ_M depend on Pr_M . The latter dissipation ratio is expected to increase with Pr_M for large-scale and small-scale dynamos in classical MHD; see Brandenburg (2014). This trend of ϵ_K / ϵ_M with Pr_M is also observed in our DNS of chiral MHD; see also bottom panel of figure 9. However, we do observe a power

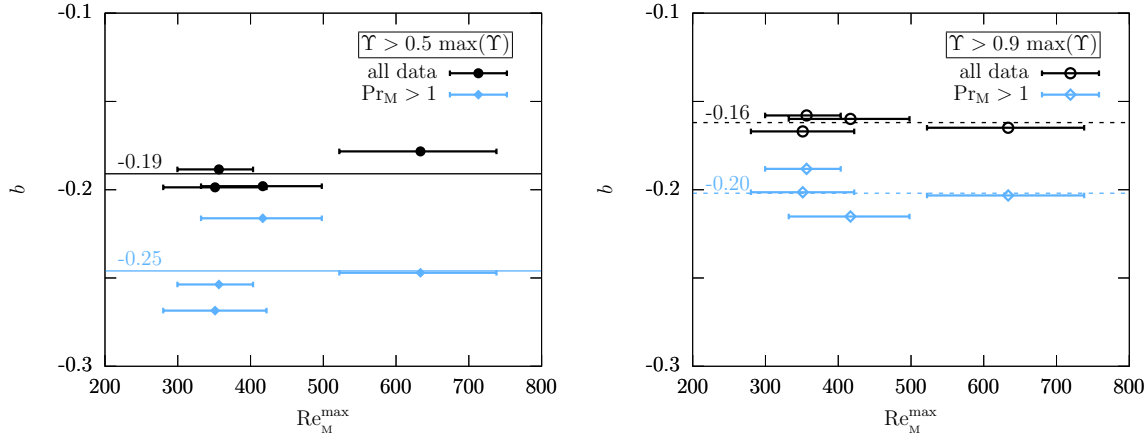


Figure 10. The slope resulting from a fit of the function $\langle \Upsilon \rangle_t = a \text{Pr}_M^b$ to the data points presented in the left panel of figure 9 as a function of the range of maximum magnetic Reynolds numbers found in simulations shown in the right panel of figure 9. The vertical bars indicate the range of Re_M^{\max} , which decreases from small to large Pr_M . Results for the fitting to all data are shown as black data points and results for using $\text{Pr}_M > 1$ as blue diamonds. Horizontal lines indicate the average values of the slopes. *Left panel:* $\langle \Upsilon \rangle_t$ has been obtained using all data with $\Upsilon > 0.5 \max(\Upsilon)$. *Right panel:* $\langle \Upsilon \rangle_t$ has been obtained using all data with $\Upsilon > 0.9 \max(\Upsilon)$.

Table 2. Fit results for $\langle \Upsilon \rangle_t = a \text{Pr}_M^b$

Run series	a (all Pr_M)	b (all Pr_M)	a ($\text{Pr}_M > 1$)	b ($\text{Pr}_M > 1$)
D (using $\Upsilon > 0.5 \max(\Upsilon)$)	0.23	-0.20	0.24	-0.22
D (using $\Upsilon > 0.9 \max(\Upsilon)$)	0.27	-0.16	0.29	-0.22
F (using $\Upsilon > 0.5 \max(\Upsilon)$)	0.23	-0.20	0.26	-0.27
F (using $\Upsilon > 0.9 \max(\Upsilon)$)	0.27	-0.17	0.29	-0.20
G (using $\Upsilon > 0.5 \max(\Upsilon)$)	0.25	-0.19	0.27	-0.25
G (using $\Upsilon > 0.9 \max(\Upsilon)$)	0.27	-0.16	0.28	-0.19
H (using $\Upsilon > 0.5 \max(\Upsilon)$)	0.25	-0.18	0.28	-0.25
H (using $\Upsilon > 0.9 \max(\Upsilon)$)	0.27	-0.17	0.29	-0.20
mean (using $\Upsilon > 0.5 \max(\Upsilon)$)	0.24	-0.19	0.26	-0.25
mean (using $\Upsilon > 0.9 \max(\Upsilon)$)	0.27	-0.16	0.29	-0.20

law scaling of $\langle \epsilon_K / \epsilon_M \rangle_t$ with Pr_M only below $\text{Pr}_M \approx 2$. For larger Prandtl numbers the ratio becomes constant.

We now perform power-law fits to the data with a function $\langle \Upsilon \rangle_t = a \text{Pr}_M^b$ with the fit parameters a and b . Both averaging conditions, using all data points for which $\Upsilon > 0.5 \max(\Upsilon)$ and $\Upsilon > 0.9 \max(\Upsilon)$, are considered. The results for the full range of Pr_M as well as for $\text{Pr}_M > 1$ can be found in table 2. Additionally, we present the slopes b as a function of the corresponding range of $\text{Re}_{M,\max}$ in figure 10. Fit results to the $\Upsilon > 0.5 \max(\Upsilon)$ condition are shown in the left and the case of $\Upsilon > 0.9 \max(\Upsilon)$ in the right panel. The obtained value of b is presented for fitting to all available data as black data points and for $\text{Pr}_M > 1$ as blue ones. We do not find a clear dependence of b on the Reynolds number range. When using data for the full Pr_M regime explored in this paper, we find mean slopes between $b = -0.16$ and $b = -0.20$. The slope of the function $\langle \Upsilon \rangle_t(\text{Pr}_M)$ becomes steeper with values between $b = -0.19$ and $b = -0.27$, when fitting only to data with $\text{Pr}_M > 1$. The latter should be a better description for the large Prandtl number regime, since the scaling of $\langle \Upsilon \rangle_t$ might change in the transition from $\text{Pr}_M < 1$ to $\text{Pr}_M > 1$.

4. Chiral magnetically driven turbulence in the early Universe

The findings from DNS presented above can be leveraged to estimate the turbulent velocities and the Reynolds number in the early Universe. As we have seen in the previous section, the ratio of kinetic to magnetic energy depends on the magnetic Prandtl number. Hence, as a first step we estimate the value of Pr_M in the early Universe. Afterwards we estimate u_{rms} and the magnetic Reynolds number for chiral magnetically driven turbulence.

4.1. Magnetic Prandtl number

The magnetic Prandtl number has been defined before as the ratio of viscosity over magnetic diffusivity. Hence it measures the relative strength of these two transport coefficients. The derivation of transport coefficients in weakly coupled high temperature gauge theories has been presented in Arnold *et al.* (2000) for various matter field content.

For the electric conductivity, Arnold *et al.* (2000) found the leading log term (converted from natural to cgs units)

$$\sigma_{\text{el}} = \frac{\kappa_{\sigma}}{4\pi \alpha \log((4\pi\alpha)^{-1/2})} \frac{k_B T}{\hbar} \quad (22)$$

with $\kappa_{\sigma} = 11.9719$ for the largest number of species considered. The magnetic resistivity in the early Universe follows as

$$\eta(T) = \frac{c^2}{4\pi \sigma_{\text{el}}} = \frac{\alpha}{\kappa_{\sigma}} \log((4\pi\alpha)^{-1/2}) \frac{\hbar c^2}{k_B T} \approx 7.3 \times 10^{-4} \frac{\hbar c^2}{k_B T} \approx 4.3 \times 10^{-9} T_{100}^{-1} \text{ cm}^2 \text{ s}^{-1}. \quad (23)$$

Here $T_{100} = 1.2 \times 10^{15}$ K, so that $k_B T_{100} = 100$ GeV.

For the shear viscosity, Arnold *et al.* (2000) report

$$\nu_{\text{shear}} = \frac{\kappa_{\text{shear}}}{\alpha^2 \log(\alpha^{-1})} \frac{(k_B T)^3}{\hbar^2 c^3} \quad (24)$$

with $\kappa_{\text{shear}} \approx 147.627$ for the largest number of species considered. The kinematic viscosity is obtained by $\nu = \nu_{\text{shear}}/\bar{\rho}$ with the mean density in the early Universe being

$$\bar{\rho} = \frac{\pi^2}{30} g_* \frac{(k_B T)^4}{\hbar^3 c^5} \approx 7.6 \times 10^{26} g_{100} T_{100}^4 \text{ g cm}^{-3}. \quad (25)$$

Dividing equation (24) by (25) we find

$$\nu = \frac{30\kappa_{\text{shear}}}{\pi^2 g_* \alpha^2 \log(\alpha^{-1})} \frac{\hbar c^2}{k_B T} \approx 1.6 \times 10^4 \frac{\hbar c^2}{k_B T} \approx 9.4 \times 10^{-2} T_{100}^{-1} \text{ cm}^2 \text{ s}^{-1}. \quad (26)$$

The ratio of equations (26) and (23) yields the magnetic Prandtl number

$$\text{Pr}_M = \frac{\nu}{\eta} \approx 2.2 \times 10^7. \quad (27)$$

4.2. Reynolds numbers

Assuming u_{rms} reaches a fraction $\Upsilon(\text{Pr}_M)$ of the saturation magnetic field strength B_{sat} , it is customary to estimate in physical units

$$u_{\text{rms}} \approx \Upsilon(\text{Pr}_M) \frac{B_{\text{sat}}}{\sqrt{4\pi\bar{\rho}}}. \quad (28)$$

The mean density in the early Universe is given in equation (25) and the value of B_{sat} depends on the chiral nonlinearity parameter

$$\lambda = 3\hbar c \left(\frac{8\alpha_{\text{em}}}{k_{\text{B}}T} \right)^2 \approx 1.3 \times 10^{-17} T_{100}^{-2} \text{ cm erg}^{-1} \quad (29)$$

and the initial chiral chemical potential μ_0 . Since the latter is unknown, we estimate it via the thermal energy density:

$$\mu_0 = \vartheta 4\alpha_{\text{em}} \frac{k_{\text{B}}T}{\hbar c} \approx 1.5 \times 10^{14} \vartheta T_{100} \text{ cm}^{-1}. \quad (30)$$

Due to the uncertainties in μ_0 we introduce the free parameter ϑ , allowing us to explore different initial conditions. The magnetic field produced by chiral dynamos as discussed in this paper reaches a maximum value of

$$B_{\text{sat}} = \left(4\pi \frac{\mu_0 k_{\lambda}}{\lambda} \right)^{1/2} \approx 6.2 \times 10^{21} \vartheta T_{100}^2 \text{ G}, \quad (31)$$

where we use as an estimate of the inverse magnetic correlation length (17), that results in

$$k_{\lambda} \approx 2.6 \times 10^{11} \vartheta T_{100} \text{ cm}^{-1}. \quad (32)$$

Following equation (28), the magnetic field drives turbulence with an rms velocity of

$$u_{\text{rms}} = 6.1 \times 10^7 \Upsilon(\text{Pr}_{\text{M}}) \vartheta \text{ cm s}^{-1}. \quad (33)$$

Finally, using equations (34), (32), and (23), we find the following value for the magnetic Reynolds number in the early Universe:

$$\text{Re}_{\text{M}} \approx \frac{u_{\text{rms}}}{k_{\lambda} \eta} \approx 5.5 \times 10^4 \Upsilon(\text{Pr}_{\text{M}}). \quad (34)$$

We stress that the size of the inertial range is independent of ϑ , and hence of μ_0 , because both, the forcing scale k_{λ} and the initial energy input scale k_{μ} , scale linear with μ_0 .

Using an extrapolation of $\Upsilon(\text{Pr}_{\text{M}}) = 0.3 \text{Pr}_{\text{M}}^{-0.2}$, motivated by DNS, see table 2, we find $\text{Re}_{\text{M}} = \mathcal{O}(10^3)$ when using $\text{Pr}_{\text{M}} = \mathcal{O}(10^7)$.

5. Conclusions

In this paper we have explored the dependence of chiral magnetically driven turbulence on initial chiral asymmetries and the magnetic Prandtl number. This process is caused by chiral MHD dynamos—an instability that originates from an asymmetry between left- and right-handed fermions and which shows mathematical similarities to classical α dynamos. However, while classical α dynamos require an energy input by turbulence, chiral dynamos can operate also in laminar flows, where they can eventually induce turbulent motions via the Lorentz force.

By solving the set of chiral MHD equations in numerical simulations, we have gained new insights into the properties of chiral magnetically driven turbulence. Our main findings from DNS may be summarized as follows:

- For a large range of parameters, it has been shown that the chiral magnetic instability generates turbulence in simulations. In this paper we have focused on the case of small chiral nonlinearity parameters λ_{μ} , defined in equation (9), where turbulence becomes strong enough to affect the evolution of the magnetic field.
- A central parameter explored in our simulations is Υ , the square root of which is the ratio of kinetic over magnetic energy; see definition in equation (20). Due to the nonlinearity of the Lorentz force, the velocity field grows at a rate that is twice the one of the magnetic

field strength. As a result, Υ increases initially as a power law. Once there is a back reaction of the velocity field on the magnetic field, Υ stays approximately constant, see e.g. the left panel of figure 6.

- For magnetic Prandtl numbers $\text{Pr}_M = 1$, the time average of Υ , taken after its exponential growth phase and referred to here as $\langle \Upsilon \rangle_t$, has been determined to be between 0.24 and 0.27. This value seems to be independent of the initial chiral asymmetry.
- For $\text{Pr}_M > 1$, Υ decreases. With our DNS we find a scaling of approximately $\Upsilon(\text{Pr}_M) = 0.3 \text{Pr}_M^{-0.2}$.
- We do not find a change of the function $\Upsilon(\text{Pr}_M)$ for different regimes of Re_M , however, only a small variation of Re_M has been considered and this might change when increasing the statistics and the extending the range of Re_M .

A chiral dynamo instability and hence chiral magnetically driven turbulence can only occur in extreme astrophysical environments, because a high temperature is required for the existence of a chiral asymmetry. At low energies chiral flipping reactions destroy any difference in number density between left- and right handed fermions. As an astrophysically relevant regime, we have discussed the plasma of the early Universe. We have presented an approximation of the magnetic Prandtl number and used it, together with our findings from DNS, to estimate the magnetic Reynolds number. We find that a value of $\text{Re}_M \mathcal{O}(10^3)$ can be expected for chiral magnetically driven turbulence, if the chiral asymmetry is generated by thermal processes.

Acknowledgements

J.S. thanks the organizers of the “2nd Conference on Natural Dynamos” for the interesting and fruitful conference held in Valtice. This project has received funding from the European Union’s Horizon 2020 research and innovation program under the Marie Skłodowska-Curie grant No. 665667. We thank for support by the École polytechnique fédérale de Lausanne, Nordita, and the University of Colorado through the George Ellery Hale visiting faculty appointment. Support through the NSF Astrophysics and Astronomy Grant Program (grants 1615100 & 1615940), the Research Council of Norway (FRINATEK grant 231444), and the European Research Council (grant number 694896) are gratefully acknowledged. Simulations presented in this work have been performed with computing resources provided by the Swedish National Allocations Committee at the Center for Parallel Computers at the Royal Institute of Technology in Stockholm.

References

- Alekseev, A.Y., Cheianov, V.V. and Fröhlich, J., Universality of Transport Properties in Equilibrium, the Goldstone Theorem, and Chiral Anomaly. *Phys. Rev. Lett.*, 1998, **81**, 3503.
- Arnold, P., Moore, G.D. and Yaffe, L.G., Transport coefficients in high temperature gauge theories (I): leading-log results. *J. High Energy Phys.*, 2000, **11**, 001.
- Biskamp, D. and Müller, W.C., Decay Laws for Three-Dimensional Magnetohydrodynamic Turbulence. *Phys. Rev. Lett.*, 1999, **83**.
- Blackman, E.G. and Brandenburg, A., Dynamic Nonlinearity in Large-Scale Dynamos with Shear. *Astrophys. J.*, 2002, **579**, 359–373.
- Boyarsky, A., Fröhlich, J. and Ruchayskiy, O., Self-Consistent Evolution of Magnetic Fields and Chiral Asymmetry in the Early Universe. *Phys. Rev. Lett.*, 2012, **108**.
- Boyarsky, A., Fröhlich, J. and Ruchayskiy, O., Magnetohydrodynamics of chiral relativistic fluids. *Phys. Rev. D*, 2015, **92**, 043004.
- Brandenburg, A., Magnetic Prandtl Number Dependence of the Kinetic-to-magnetic Dissipation Ratio. *Astrophys. J.*, 2014, **791**, 12.

- Brandenburg, A. and Dobler, W., Hydromagnetic turbulence in computer simulations. *Comp. Phys. Comm.*, 2002, **147**, 471–475.
- Brandenburg, A., Enqvist, K. and Olesen, P., Large-scale magnetic fields from hydromagnetic turbulence in the very early universe. *Phys. Rev. D*, 1996, **54**.
- Brandenburg, A., Kahniashvili, T., Mandal, S., Pol, A.R., Tevzadze, A.G. and Vachaspati, T., Evolution of hydromagnetic turbulence from the electroweak phase transition. *Phys. Rev. D*, 2017a, **96**, 123528.
- Brandenburg, A., Kahniashvili, T. and Tevzadze, A.G., Nonhelical Inverse Transfer of a Decaying Turbulent Magnetic Field. *Phys. Rev. Lett.*, 2015, **114**, 075001.
- Brandenburg, A., Schober, J., Rogachevskii, I., Kahniashvili, T., Boyarsky, A., Fröhlich, J., Ruchayskiy, O. and Kleorin, N., The turbulent chiral-magnetic cascade in the early universe. *ApJL*, 2017b, **845**, L21.
- Brandenburg, A., Computational aspects of astrophysical MHD and turbulence; in *Advances in Nonlinear Dynamics*, edited by A. Ferriz-Mas and M. Núñez, 2003, pp. 269–344.
- Dermer, C.D., Cavadini, M., Razzaque, S., Finke, J.D., Chiang, J. and Lott, B., Time Delay of Cascade Radiation for TeV Blazars and the Measurement of the Intergalactic Magnetic Field. *Astrophys. J. Lett.*, 2011, **733**, L21.
- Field, G.B. and Carroll, S.M., Cosmological magnetic fields from primordial helicity. *Phys. Rev. D*, 2000, **62**.
- Fröhlich, J. and Pedrini, B., New applications of the chiral anomaly; in *Mathematical Physics 2000*, edited by A.S. Fokas, A. Grigoryan, T. Kibble and B. Zegarlinski, International Conference on Mathematical Physics 2000, Imperial college (London), 2000.
- Fröhlich, J. and Pedrini, B., Axions, quantum mechanical pumping, and primeval magnetic fields; in *Statistical Field Theory*, edited by A. Cappelli and G. Mussardo, 2002.
- Fukushima, K., Kharzeev, D.E. and Warringa, H.J., The Chiral Magnetic Effect. *Phys. Rev. D*, 2008, **78**, 074033.
- Grasso, D. and Rubinstein, H.R., Magnetic fields in the early Universe. *Phys. Rep.*, 2001, **348**, 163.
- Joyce, M. and Shaposhnikov, M., Primordial Magnetic Fields, Right Electrons, and the Abelian Anomaly. *Phys. Rev. Lett.*, 1997, **79**, 1193.
- Kahniashvili, T., Tevzadze, A.G., Brandenburg, A. and Neronov, A., Evolution of primordial magnetic fields from phase transitions. *Phys. Rev. D*, 2013, **87**, 083007.
- Kazantsev, A.P., Enhancement of a Magnetic Field by a Conducting Fluid. *Soviet Journal of Experimental and Theoretical Physics*, 1968, **26**, 1031.
- Kemel, K., Brandenburg, A. and Ji, H., Model of driven and decaying magnetic turbulence in a cylinder. *Phys. Rev. E*, 2011, **84**, 056407.
- Kharzeev, D.E., McLerran, L.D. and Warringa, H.J., The Effects of topological charge change in heavy ion collisions: 'Event by event P and CP violation'. *Nucl. Phys.*, 2008, **A803**, 227.
- Kleeorin, N. and Ruzmaikin, A., Dynamics of the average turbulent helicity in a magnetic field. *Magnetohydrodynamics No. 2*, 1982, **2**, 17–24.
- Krause, F. and Rädler, K.H., *Mean-Field Magnetohydrodynamics and Dynamo Theory*, 1980 (Pergamon, Oxford).
- Kulsrud, R.M. and Anderson, S.W., The spectrum of random magnetic fields in the mean field dynamo theory of the Galactic magnetic field. *Astrophys. J.*, 1992, **396**, 606.
- Kulsrud, R.M. and Zweibel, E.G., On the origin of cosmic magnetic fields. *Rep. Prog. Phys.*, 2008, **71**, 046901.
- Moffatt, H.K., *Magnetic Field Generation in Electrically Conducting Fluids*, 1978 (Cambridge, England, Cambridge University Press).
- Neronov, A. and Vovk, I., Evidence for Strong Extragalactic Magnetic Fields from Fermi Observations of TeV Blazars. *Science*, 2010, **328**, 73.
- Parker, E.N., Hydromagnetic Dynamo Models. *Astrophys. J.*, 1955, **122**, 293.
- Redlich, A.N. and Wijewardhana, L.C.R., Induced Chern-Simons terms at high temperatures and finite densities. *Phys. Rev. Lett.*, 1985, **54**, 970.
- Rogachevskii, I., Ruchayskiy, O., Boyarsky, A., Fröhlich, J., Kleeorin, N., Brandenburg, A. and Schober, J., Laminar and turbulent dynamos in chiral magnetohydrodynamics-I: Theory. *Astrophys. J.*, 2017, **846**, 153.
- Schober, J., Rogachevskii, I., Brandenburg, A., Boyarsky, A., Fröhlich, J., Ruchayskiy, O. and Kleeorin, N., Laminar and turbulent dynamos in chiral magnetohydrodynamics. II. Simulations. *arXiv:1711.09733*, 2017.
- Son, D.T. and Surowka, P., Hydrodynamics with Triangle Anomalies. *Phys. Rev. Lett.*, 2009, **103**, 191601.
- Steenbeck, M., Krause, F. and Rädler, K.H., Berechnung der mittleren Lorentz-Feldstärke $\overline{\mathbf{v} \times \mathbf{B}}$ für ein elektrisch leitendes Medium in turbulenter, durch Coriolis-Kräfte beeinflusster Bewegung. *Zeitschrift Naturforschung Teil A*, 1966, **21**, 369.
- Subramanian, K., The origin, evolution and signatures of primordial magnetic fields. *Rep. Prog. Phys.*, 2016, **79**, 076901.
- Tsokos, K., Topological mass terms and the high temperature limit of chiral gauge theories. *Phys. Lett. B*, 1985, **157**, 413.
- Vilenkin, A., Equilibrium parity violating current in a magnetic field. *Phys. Rev. D*, 1980, **22**, 3080–3084.
- Zrake, J., Inverse Cascade of Nonhelical Magnetic Turbulence in a Relativistic Fluid. *Astrophys. J. Lett.*, 2014, **794**, L26.